Supplementary Information (SI) for Lab on a Chip.

Estimating single-cell elastic modulus in a serial microfluidic cytometer from time-of-flight and fluorescence signals analysis

Supplement

Graylen R. Chickering, Leroy L. Jia, Matthew DiSalvo, Megan A. Catterton,
Paul N. Patrone, Eric M. Darling, Gregory A. Cooksey

Supplemental Methods

Model Derivation

In this section, we derive Eq. (1) of the main text. Herein we follow the analysis of *Ref: Tam & Hyman, "Transverse motion of an elastic sphere in a shear field", J. Fluid Mech. (1973)*, which describes how elastic particles can experience a lift force that pushes them closer to the center of the channel, thus enhancing speed. This is consistent with experimental observations of the main document: time-of-flight decreases with elasticity.

The ingredients and assumptions of our model are as follows.

- The time of flight, τ, is the distance d traveled by the particle divided by its speed U

$$\tau = \frac{d}{U}. \tag{1}$$

  Considering, for example a typical value of d = 11.8 mm, the characteristic speed of particles is approximately 0.1 m/s.

- The flow field is approximately shear flow, which amounts to the assumption that the particle is small relative to the characteristic dimensions of the microfluidic channel. In particular, let y be the vertical coordinate relative to the center of the particle and perpendicular to the direction of translation, and β be the shear rate. Then the fluid velocity in the volume occupied by the particle (were it not there) is given by

$$U(y) = U_\infty + \beta y, \tag{2}$$

  where U_∞ is the average velocity of the volume infinitely far away in the direction of translation.

- The Reynolds number is small enough to ignore inertia. For this system, one typically finds that $Re_p \approx 3$. While this nominally means that inertial and viscous effects are on the same scale, we anticipate that ignoring the former still leads to semi-quantitative results, which are borne out by agreement between the model and data.

- The solid is incompressible (Poisson's ratio $\nu = 1/2$). In practice, we find that the Poisson ratio is actually around 0.44, which we expect should introduce at most a 10% error in our approximation.

- Small deformations: linear elasticity and first-order perturbation theory are valid.

- The lift force depends on various parameters (see Tam & Hyman, Eqn. 40) including the particle radius a, far-field velocity U_∞, chamber radius R, shear rate β, local vorticity ω, fluid viscosity μ, and Lamé parameters λ (bulk modulus minus 2/3 times the shear modulus) and G (shear modulus). The expression is rather complicated, so we make some more simplifying assumptions:

Under these assumptions, according to Tam & Hyman, one finds the following.

- Because the solid is incompressible,

$$\lambda \to \infty \text{ and } G = \frac{E}{3}, \tag{3}$$

where E is Young's modulus.

- Torque is balanced so the local shear rate matches the vorticity, i.e.,

$$\omega = -\frac{\beta}{2} \tag{4}$$

- The lift force is proportional to the vertical drift (height) of the particle, i.e.,

$$F_L \propto y. \tag{5}$$

Because the constant of proportionality is unknown, we can express it as some number, c, divided by β^2 without loss of generality. One also finds that the lift force is approximated by the expression

$$F_L = \frac{21\pi\mu^2 U_\infty a\beta}{2 \quad E}. \tag{6}$$

The salient part is the scaling $F_L \propto a/E$. Combining this with Eqn. (5) and the aforementioned freedom to choose the proportionality constant, we can write $y = ca/\beta E$, where c absorbs all remaining constants. As the radius increases or the elasticity decreases, the lift increases, and the particle drifts further away from its usual position and into faster streamlines. The time of flight consequently decreases. Substituting $y = ca/\beta E$ into Eqn. (2) and then substituting the resulting expression for U into Eqn. (1) yields a time of flight of

$$\tau = \frac{d}{U_\infty + c\frac{a}{E}} \tag{7}$$

in the regime where these assumptions are valid. The unknown constant c can be determined by fitting. Note that a is the radius in Tam & Hyman, but since we consider particular diameters, we let a represent diameter below. Since c is an unknown constant that will be found through regression, this redefinition does not affect our formulas. Note that in the limit of a rigid particle, $E \to \infty$, we see that the time of flight simply is

$$\tau_\infty = \frac{d}{U_\infty}. \tag{8}$$

Thus, the rigid particle time of flight τ_∞ can be used to determine U_∞.

By rearranging Eqn. 7, we obtain the following equation for the particle Young's modulus:

$$E = \frac{ca}{\frac{d}{\tau} - U_\infty}. \tag{9}$$

To determine *c*, we fit Eqn. 7 according to the process described in the next section, using the mean time of flight, mean elasticity, and mean particle diameter for each population as inputs to the regression.

Gaussian Process Regression

Ref: Rasmussen & Williams, Gaussian Processes for Machine Learning, MIT Press (2006)

The model given by Eq. 7 exhibits on the order of 10 % error relative to the data. We anticipate that this is due to both uncertainty in the data and model-form error associated with the assumptions underlying Eqn. 7.

To quantify such effects, we use Gaussian process regression (GPR) to account for both systematic and random effects. In particular, we postulate a Gaussian process prior GP($m(x)$,$k(x,x')$); here, each data point x consists of a time of flight τ and a diameter a (two independent variables). The deterministic mean $m(x) = E(\tau,a)$ is given by Eqn. 7, and its unspecified parameters are determined as part of the GPR described below. For the covariance function, we use the standard radial basis function

$$k(x,x') = \sigma_f^2 exp\left[-\frac{(\tau-\tau')^2}{2l_\tau^2} - \frac{(a-a')^2}{2l_a^2}\right] \tag{10}$$

where $x = (\tau,a)$ and $x' = (\tau',a')$. The parameters σ_f (scale factor), ℓ_τ (length scale for τ variable), and ℓ_a (length scale for a variable) control the wiggliness of the fit and are found via optimization.

From Rasmussen & Williams, the posterior (i.e., "corrected") mean is

$$\bar{f}_* = m(X_*) + K(X_*,X)\left[K(X,X) + \sigma_n^2 I\right]^{-1}(y - m(X)) \tag{11}$$

where σ_n^2 is the variance of the noise associated with y, and the posterior variance (i.e., uncertainty in the mean) is

$$cov(f_*) = K(X_*,X_*) - K(X_*,X)[K(X,X) + \sigma_n^2 I]^{-1}K(X,X_*) \tag{12}$$

In the notation of Rasmussen & Williams, X is the list of data inputs (i.e. particle diameters and elasticities) at which measurements were performed, and X_* is the list of test inputs at we wish to estimate the TOF. Similarly, y denotes the training outputs (i.e. measured time of flight data) and f_* denotes the test outputs that we wish to estimate at the X_*.

We estimate the hyperparameters ℓ_τ, ℓ_a, and σ_f as those that optimize the marginal likelihood (the probability of generating a certain observed sample given certain parameters). Let θ =

($\sigma_f, \ell_\tau, \ell_a$) be the parameters associated with the covariance function and let c be the parameter for the mean function, given previously in Eqn. 7. For a GP,

$$\log p(y|X,\theta,c) = -\frac{1}{2}(y-m)^T\left(K+\sigma_n^2 I\right)^{-1}(y-m) - \frac{1}{2}\det\left(K+\sigma_n^2 I\right) - \frac{n}{2}\log 2\pi \tag{13}$$

Taking derivatives, we are led to the system of four equations

$$\frac{\partial}{\partial\theta_j}\log p(y|X,\theta,c) = \frac{1}{2}tr\left[\left(\alpha\alpha^T - K^{-1}\right)\frac{\partial K}{\partial\theta_j}\right] = 0, j = 1, 2, 3 \tag{14}$$

$$\frac{\partial}{\partial c}\log p(y|X,\theta,c) = (y-m)^T\left(K+\sigma_n^2 I\right)^{-1}\frac{\partial m}{\partial c} = 0 \tag{15}$$

where $\alpha = K^{-1}(y-m)$. For reference, we found that

$$\frac{\partial K}{\partial \sigma_f} = 2\sigma_f \exp\left[-\frac{(\tau-\tau')^2}{2l_\tau^2} - \frac{(a-a')^2}{2l_a^2}\right] \tag{16}$$

$$\frac{\partial K}{\partial l_\tau} = \sigma_f^2 \exp\left[-\frac{(\tau-\tau')^2}{2l_\tau^2} - \frac{(a-a')^2}{2l_a^2}\right]\frac{(\tau-\tau')^2}{l_\tau^3} \tag{17}$$

$$\frac{\partial K}{\partial l_a} = \sigma_f^2 \exp\left[-\frac{(\tau-\tau')^2}{2l_\tau^2} - \frac{(a-a')^2}{2l_a^2}\right]\frac{(a-a')^2}{l_a^3} \tag{18}$$

$$\frac{\partial m}{\partial c} = \frac{a}{\frac{d}{\tau_\infty} - U_\infty} \tag{19}$$

The equations are then solved numerically.

Supplemental Results and Discussion

Modeling

Figures 1, 2, and 3 illustrate the regression surface and associated uncertainty in the predicted Young's modulus as a function of τ and a in time-of-flight (TOF) from regions 1-2, 2-3, and 3-4, respectively. The region 1-2 model was not used.

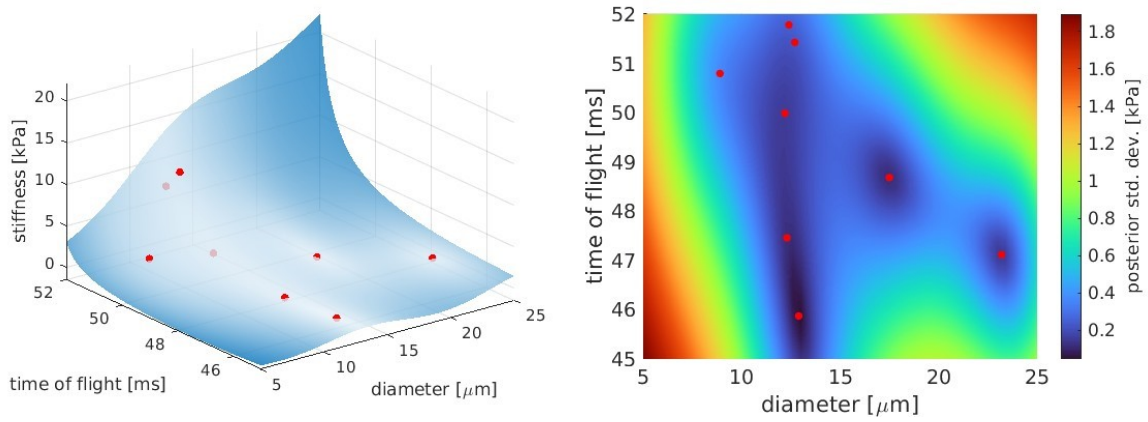

Figure S1: (Left) Predicted Young's modulus as a function of particle time of flight and diameter in region 1. (Right) Standard deviation associated with elasticity prediction.

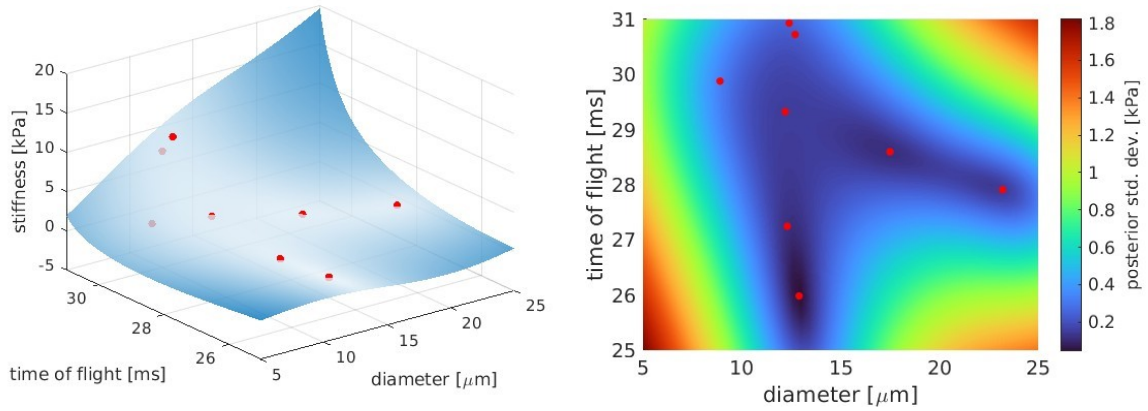

Figure S2: (Left) Predicted Young's modulus as a function of particle time of flight and diameter in region 2. (Right) Standard deviation associated with elasticity prediction.

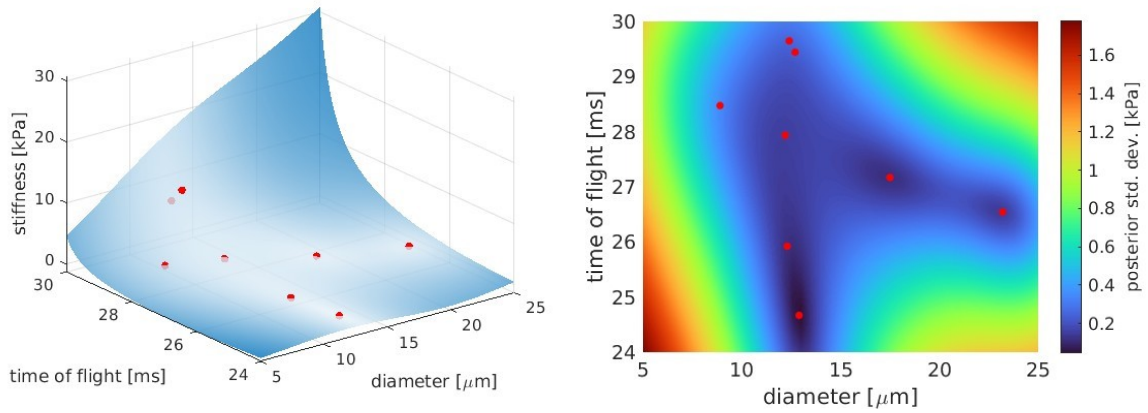

Figure S3: (Left) Predicted Young's modulus as a function of particle time of flight and diameter in region 3. (Right) Standard deviation associated with elasticity prediction.

Characterization of TOF

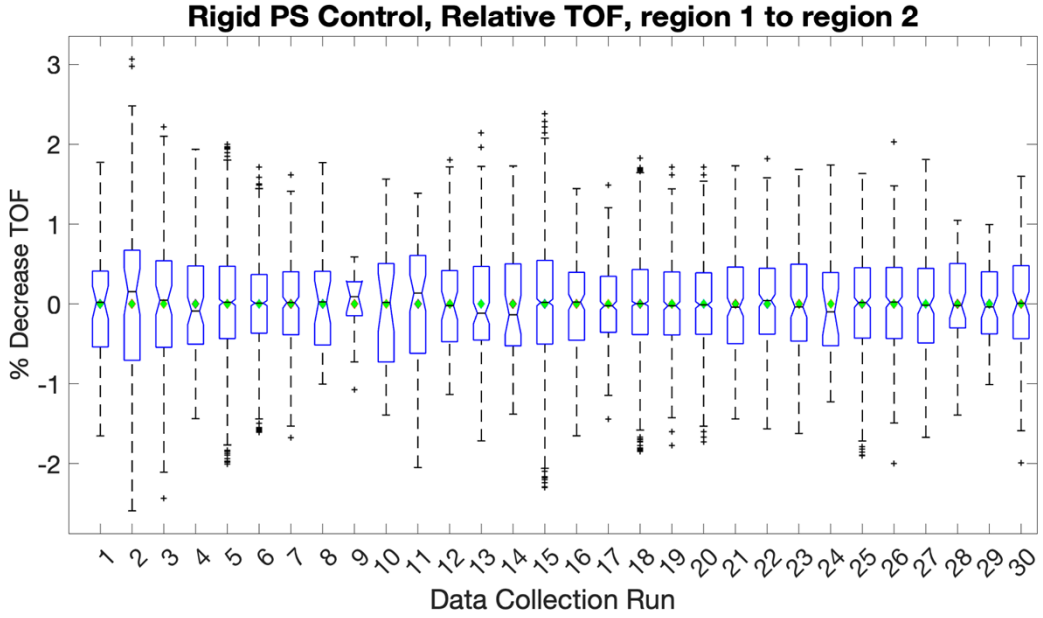

Figure S4: Spread in the decrease in region 1 to 2 TOF of the control population from individual data collection runs. Relative decrease in TOF for control particles is ideally 0 %. Means are marked with green diamonds. Outliers have not been removed.

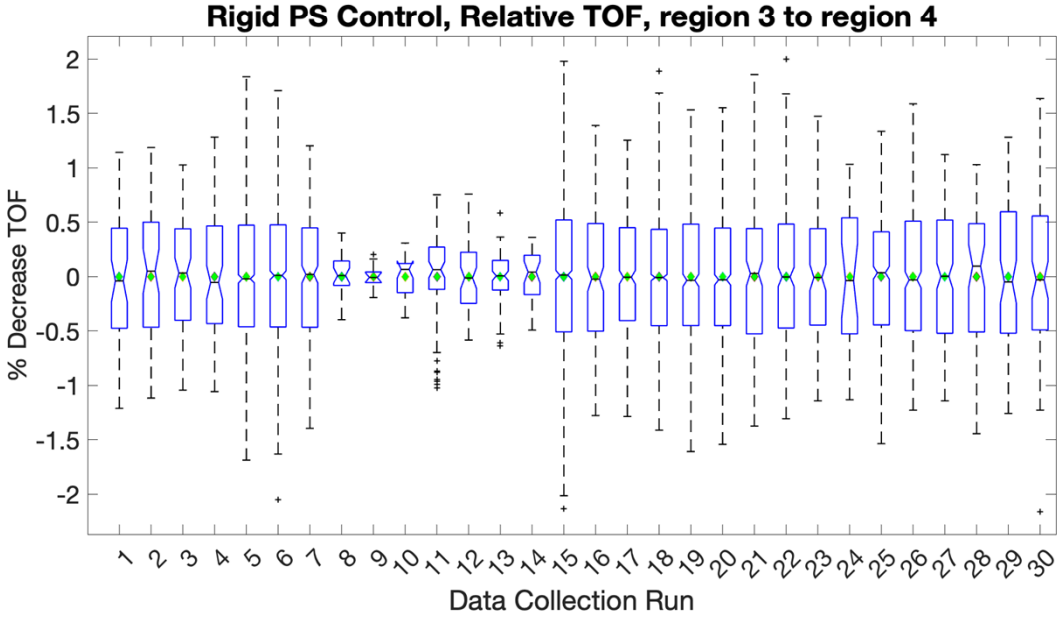

Figure S5: Spread in the decrease in region 3 to 4 TOF of the control population from individual

data collection runs. Relative decrease in TOF for control particles is ideally 0 %. Means are marked with green diamonds. Outliers have not been removed.

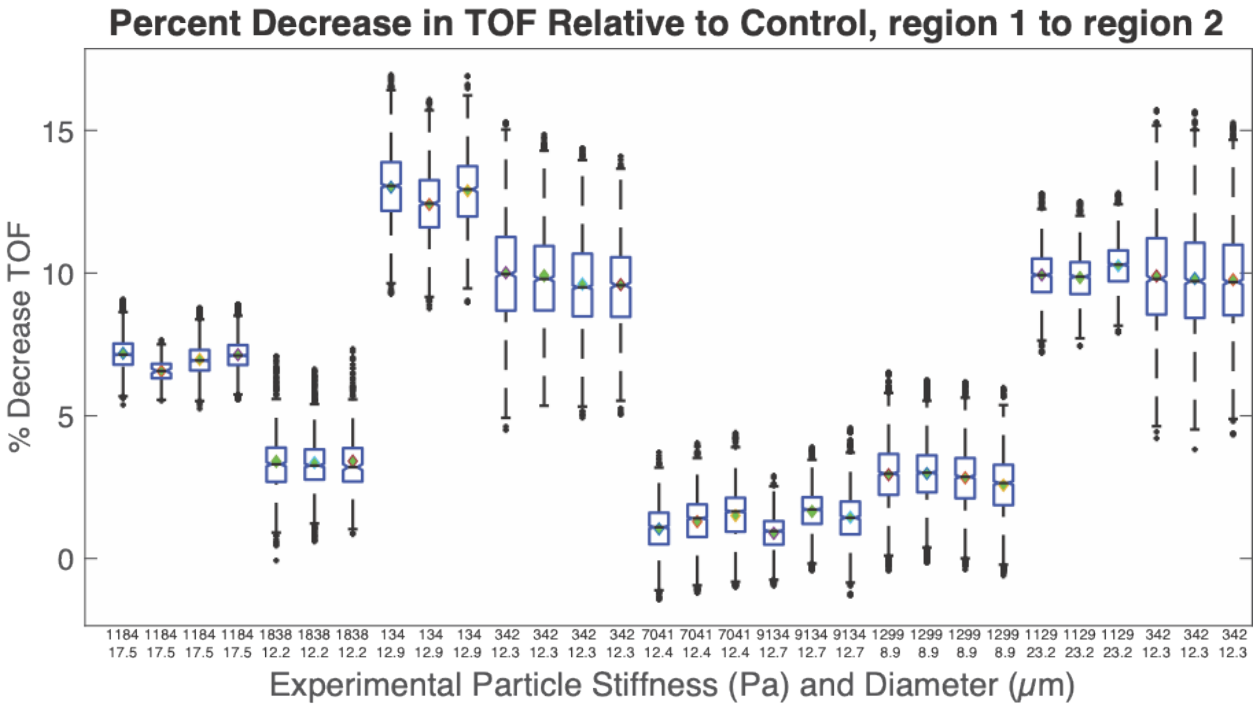

Figure S6: Decrease in region 1 to 2 TOF for experimental particles relative to control. Population means are marked with green diamonds. Runs of the same experimental particle are grouped. X-axis labels of elastic modulus (Pa, top row) and diameter (μm, bottom row) are nominal.

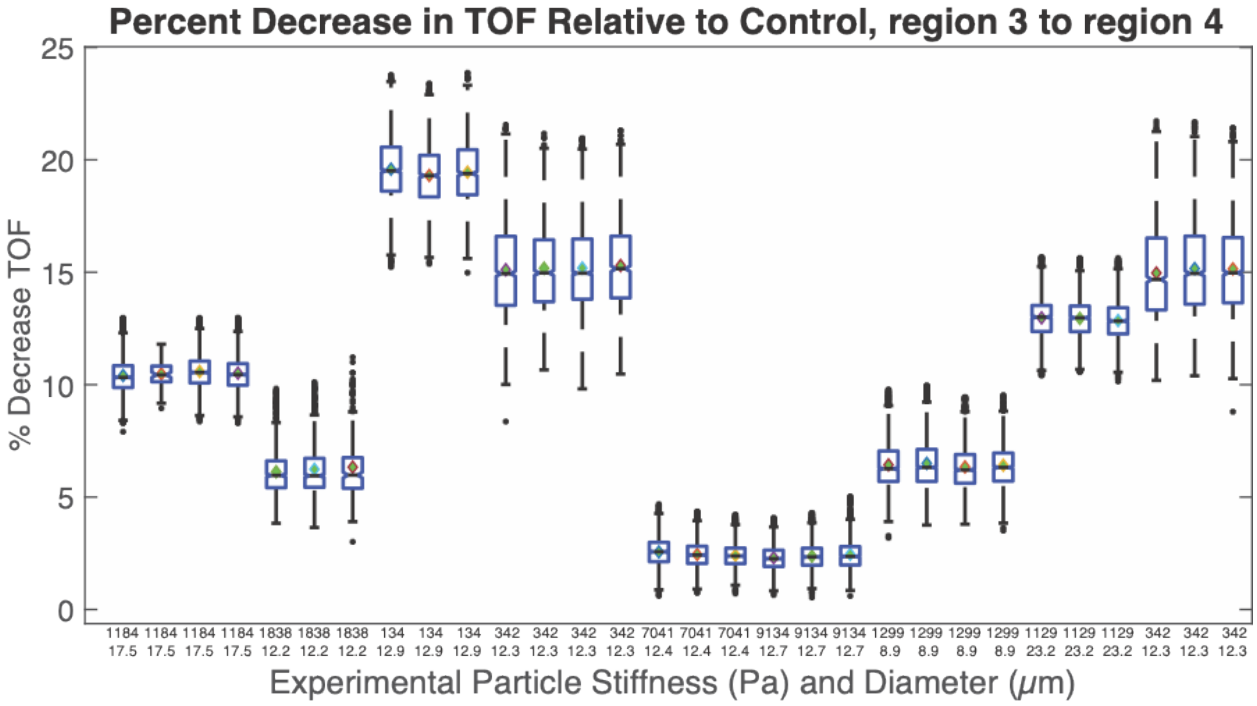

Figure S7: Decrease in region 3 to 4 TOF for experimental particles relative to control. Population

means are marked with green diamonds. Runs of the same experimental particle are next to one another. X-axis labels of elastic modulus (Pa, top row) and diameter (μm, bottom row) are nominal.

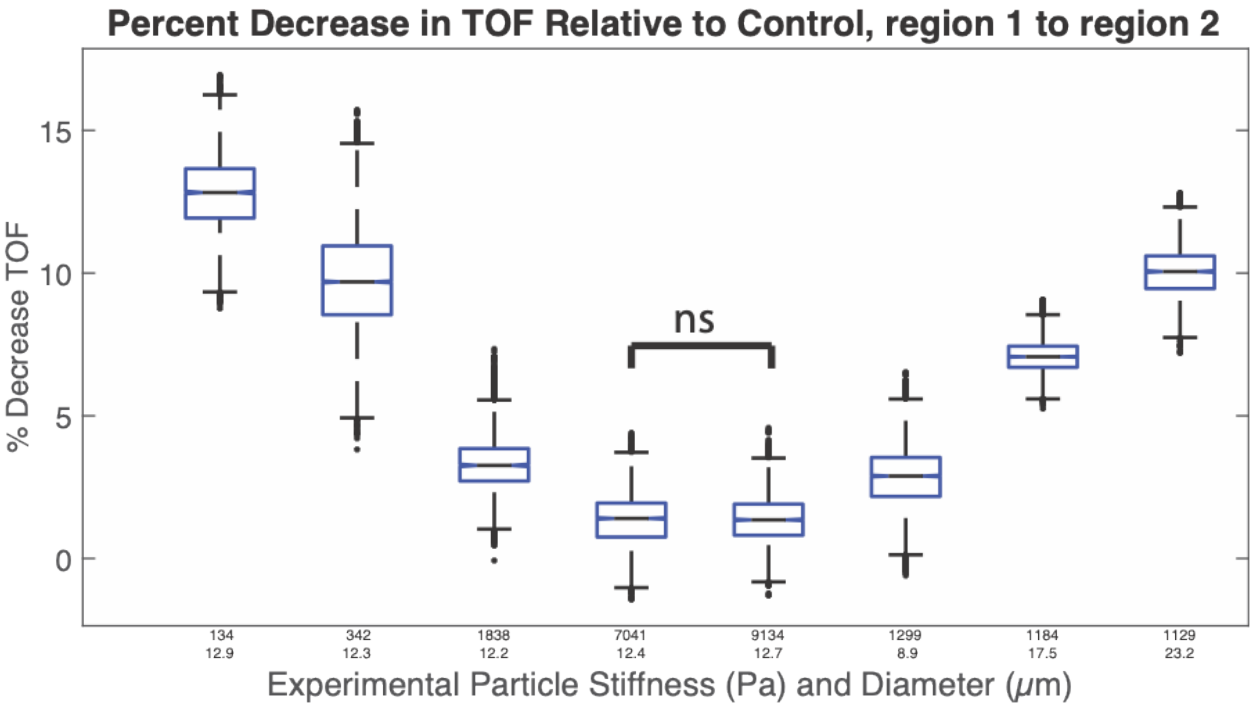

Figure S8: Decrease in relative region 1 to 2 TOF for experimental particles after pooling runs by population. X-axis labels of elastic modulus (Pa, top row) and diameter (μm, bottom row) are nominal. Unless otherwise noted, populations are significantly different ($p << 0.0001$).

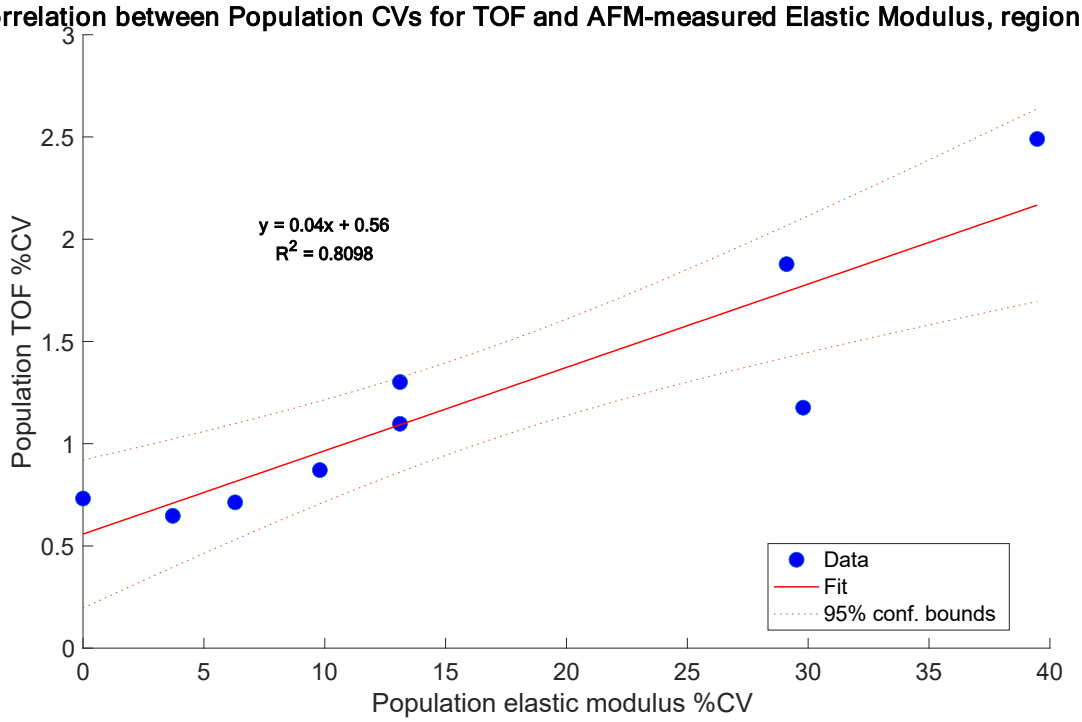

Figure S9: Correlation between population coefficients of variation (CVs) in relative region 3 to 4 TOF change and CVs in population atomic force microscopy (AFM) elastic modulus measurements.

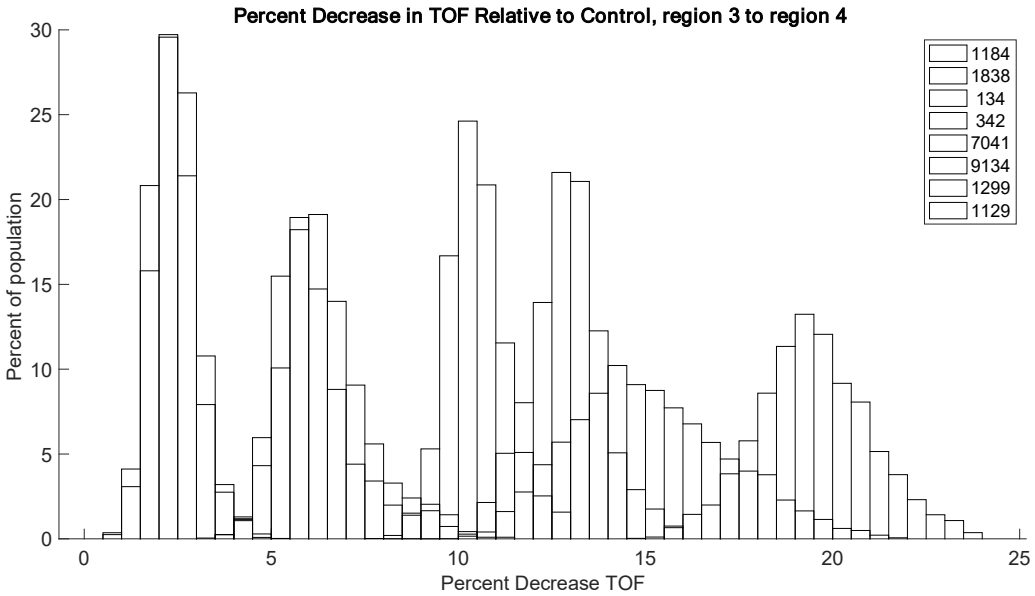

Figure S10: Histogram view of relative decrease in region 3 to 4 TOF for experimental particle populations. Runs of same particle lot were pooled. Legend lists nominal elastic moduli (Pa) for the populations.

The variation in TOF of the control population is greater at the beginning of the chip (Fig. S4) compared to later in the device (Fig. S5). The largest population CV of an individual run was 1.2 % for regions 1-2; no other variation of the control population for any run or any region exceeded 1.0 % CV. This suggests the particles may not have fully migrated to their equilibrium positions or that the flow is still stabilizing.

Additionally, variation in TOF from different runs of the same experimental population is greater at region 1 to 2 (Fig. S6) than region 3 to 4 (Fig. S7). While per-particle CVs are still impressively tight, as shown in the main text Fig. 4b, values from the first region of the chip have higher error and variability. Between region 1 and 2, the relative decrease in TOF of experimental particles ranged from -1.4 % to 17 % (Fig. S6). From region 2 to 3, this range was 0.40 % to 22 %. Finally, from region 3 to 4, the range was 0.50 % to 24 % (Fig. S7), suggesting a slight increase in resolution or sensitivity at later regions as a consequence of particles reaching a more stable position in the flow. Grouping runs of the same lot together, all results were significant ($p << 0.0001$) across all regions except for excluding 7.0 kPa vs 9.1 kPa lots from region 1 to 2 (Fig. S8).

Figures 9 and 10 provide additional comparisons between relative TOF and population characteristics. Populations measured with greater variation in TOF also tend to have greater variation in elastic modulus.

Characterization of STA metrics: instantaneous velocity

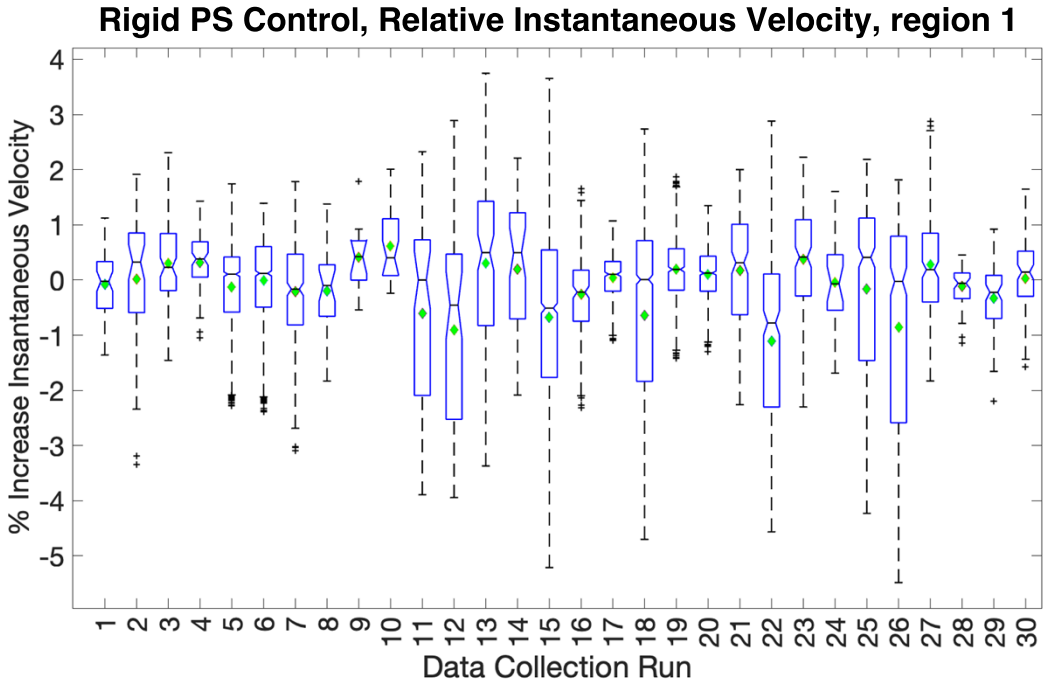

Figure S11: Spread in the increase in region 1 instantaneous velocity of the control population from individual data collection runs. Relative decrease in instantaneous velocity for control particles is ideally 0 %. Means are marked with green diamonds.

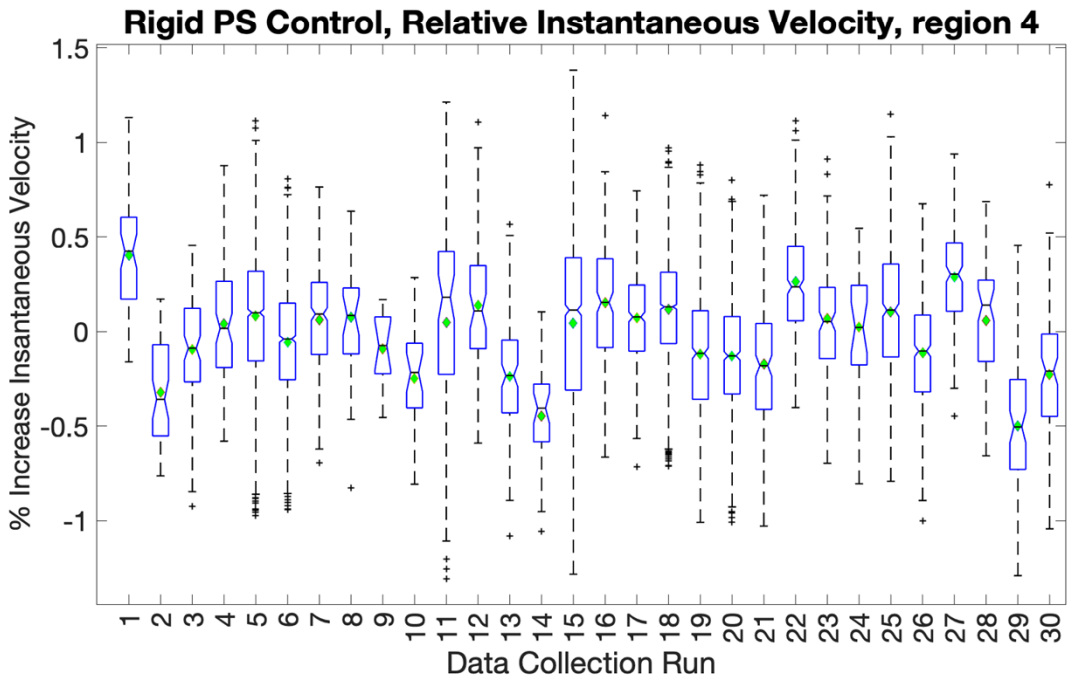

Figure S12: Spread in the increase in region 4 instantaneous velocity of the control population from individual data collection runs. Relative decrease in instantaneous velocity for control particles is ideally 0 %. Means are marked with green diamonds.

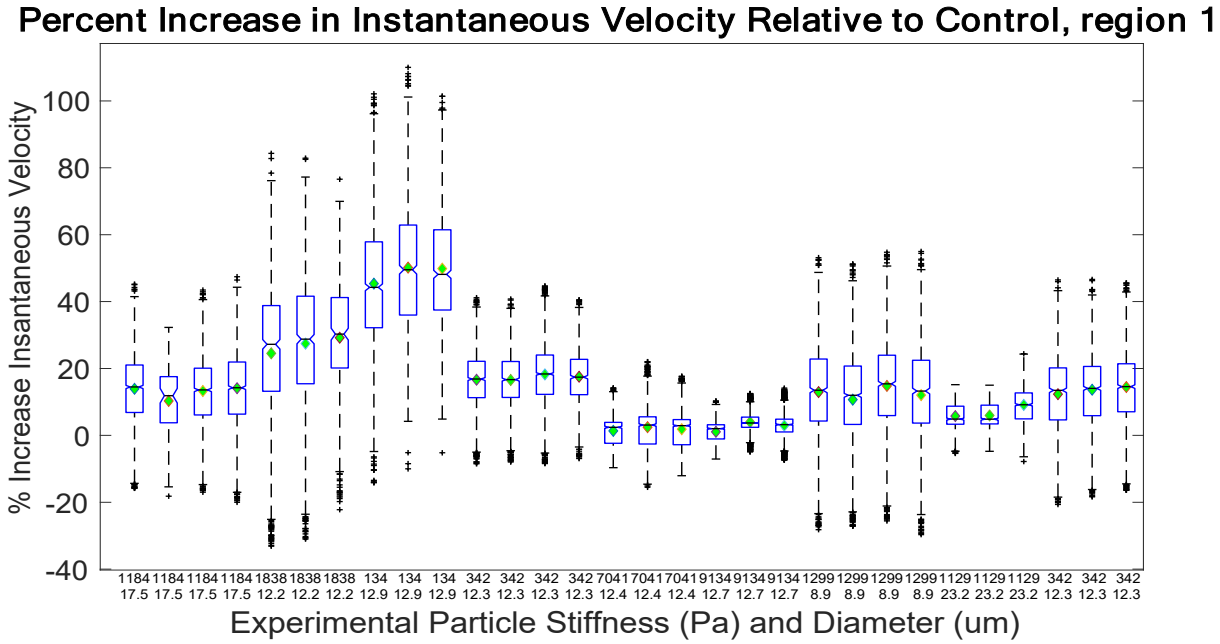

Figure S13: Increase in region 1 instantaneous velocity for experimental particles relative to control. Population means are marked with green diamonds. Runs of the same experimental particle are next to one another. X-axis labels of elastic modulus (Pa, top row) and diameter (μm, bottom row) are nominal.

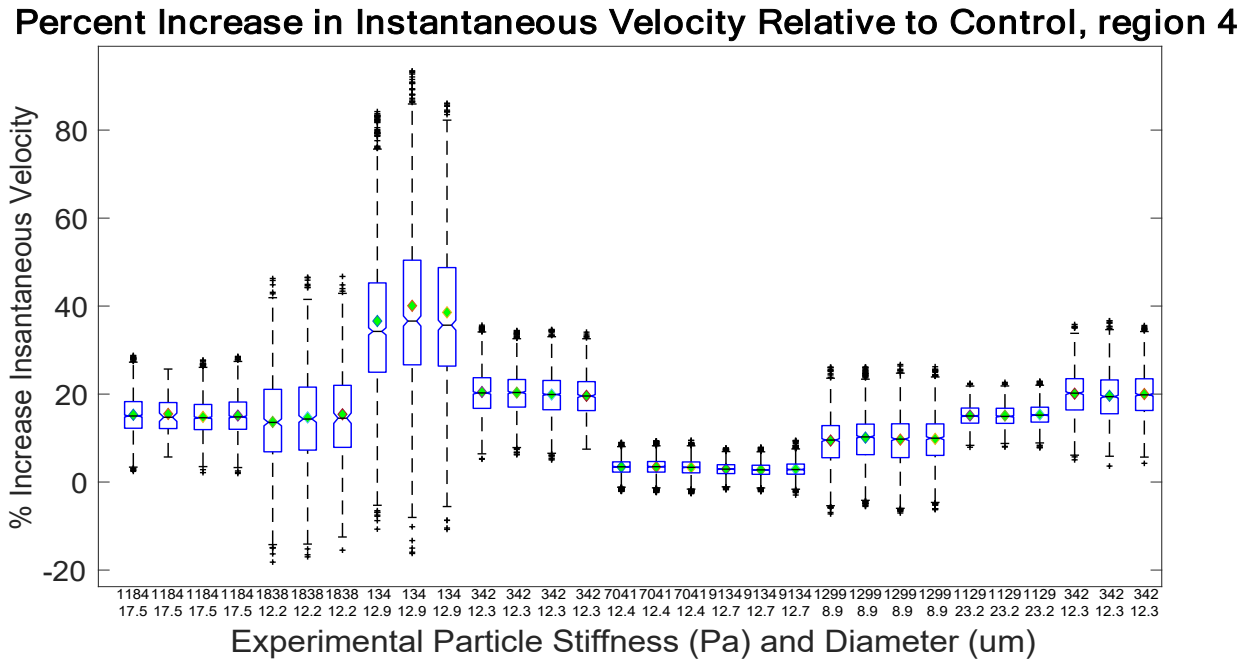

Figure S14: Increase in region 4 instantaneous velocity for experimental particles relative to control. Population means are marked with green diamonds. Runs of the same experimental particle are next to one another. X-axis labels of elastic modulus (Pa, top row) and diameter (μm, bottom row) are nominal.

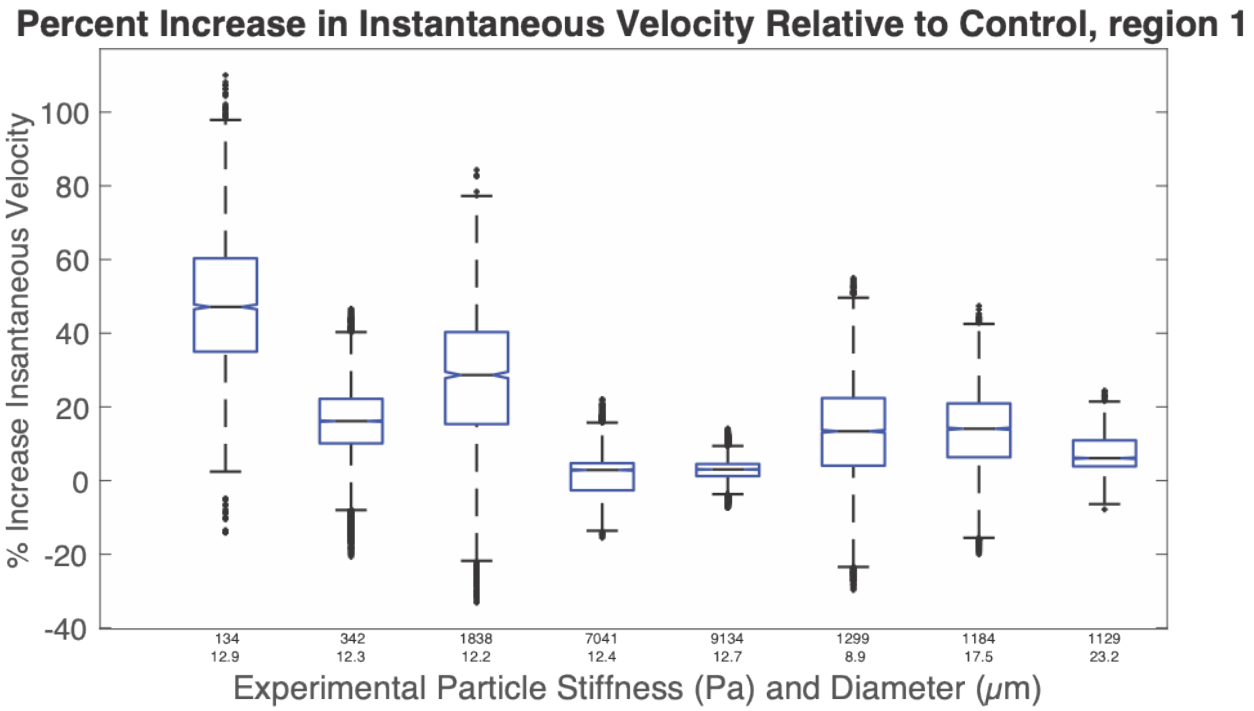

Figure S15: Increase in relative region 1 instantaneous velocity for experimental particles after pooling runs by population. X-axis labels of elastic modulus (Pa, top row) and diameter (μm, bottom row) are nominal. Unless otherwise noted, populations are significantly different ($p < 0.001$).

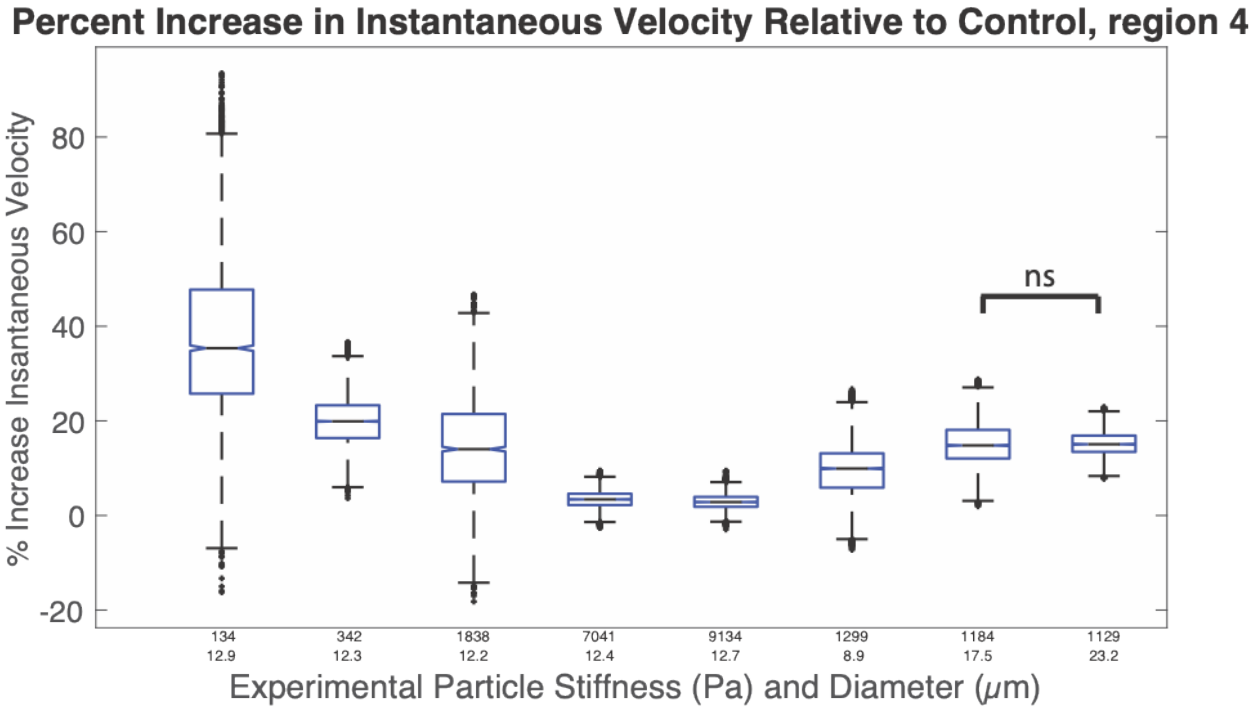

Figure S16: Increase in relative region 4 instantaneous velocity for experimental particles after pooling runs by population. X-axis labels of elastic modulus (Pa, top row) and diameter (μm, bottom row) are nominal. Unless otherwise noted, populations are significantly different ($p < 0.001$).

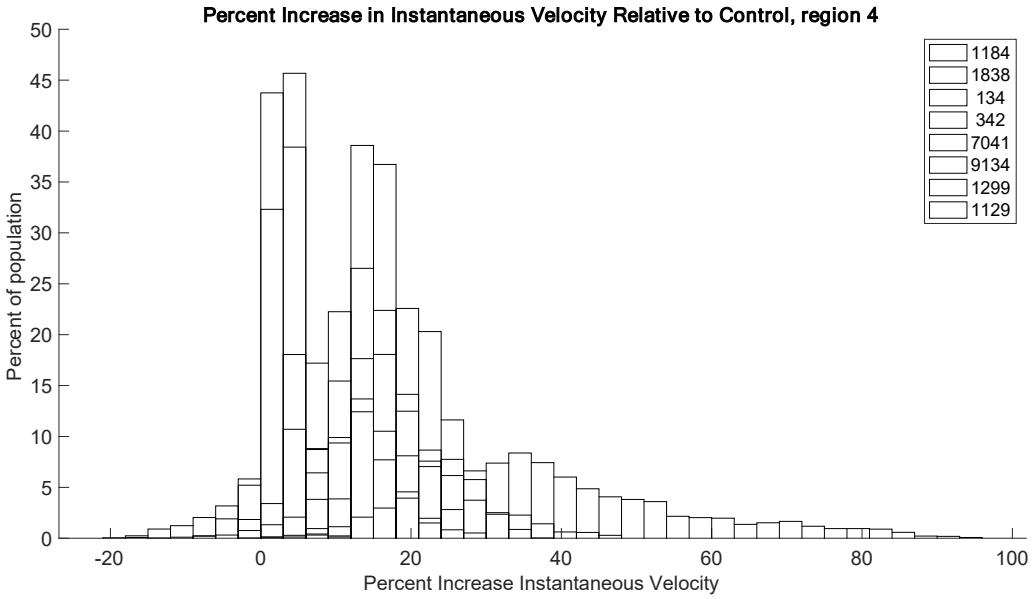

Figure S17: Histogram view of relative increase in region 4 instantaneous velocity for experimental particle populations. Runs of same particle lot were pooled. Legend lists nominal elastic moduli (Pa) for the populations.

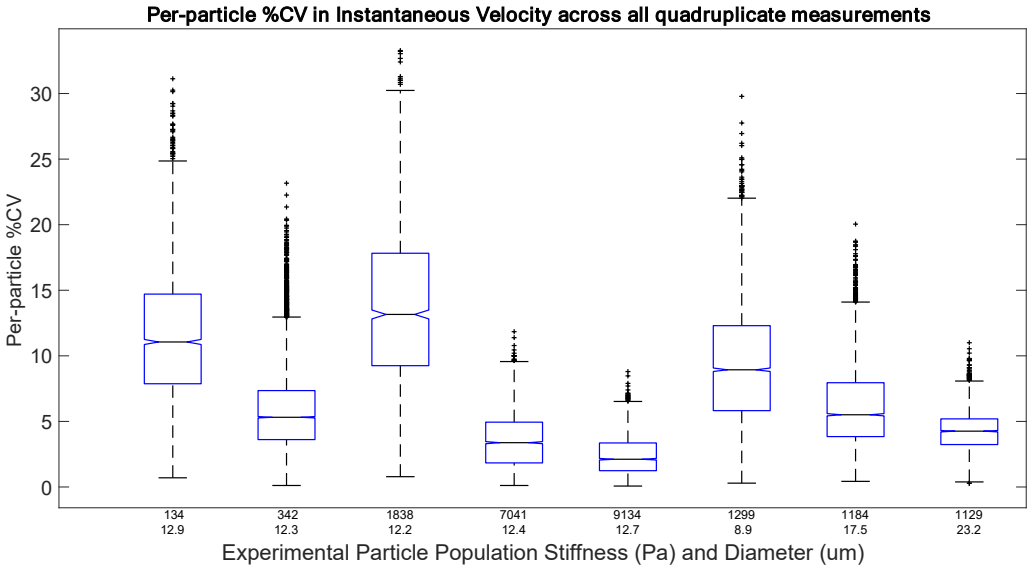

Figure S18: Per-particle CV in region 1 through 4 instantaneous velocity measurements. Individual particles CVs are grouped into boxes by particle lot. X-axis labels of elastic modulus (Pa, top row) and diameter (μm, bottom row) are nominal.

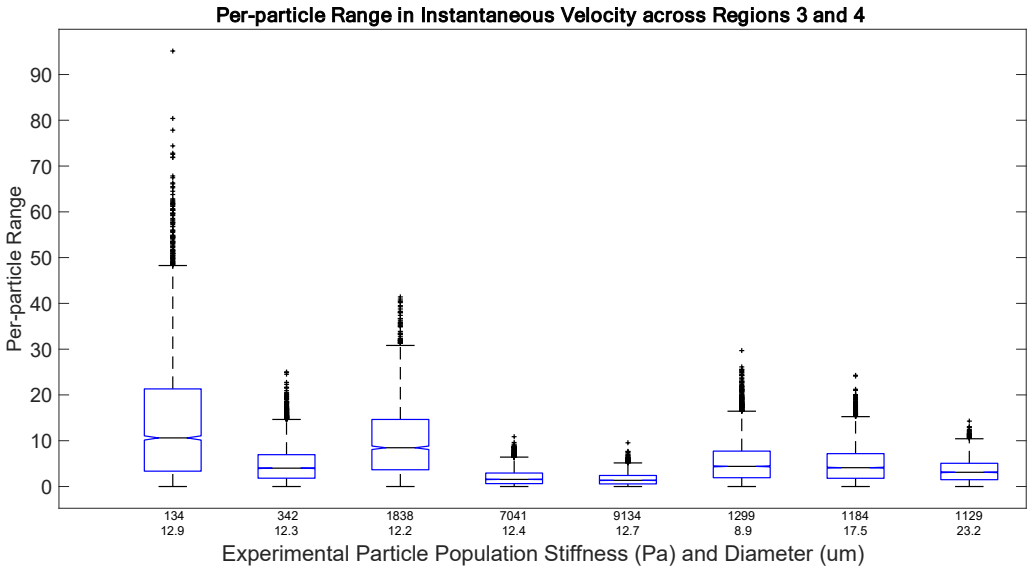

Figure S19: Per-particle range between region 3 and 4 instantaneous velocity measurements. Individual particles CVs are grouped into boxes by particle lot. X-axis labels of elastic modulus (Pa, top row) and diameter (μm, bottom row) are nominal.

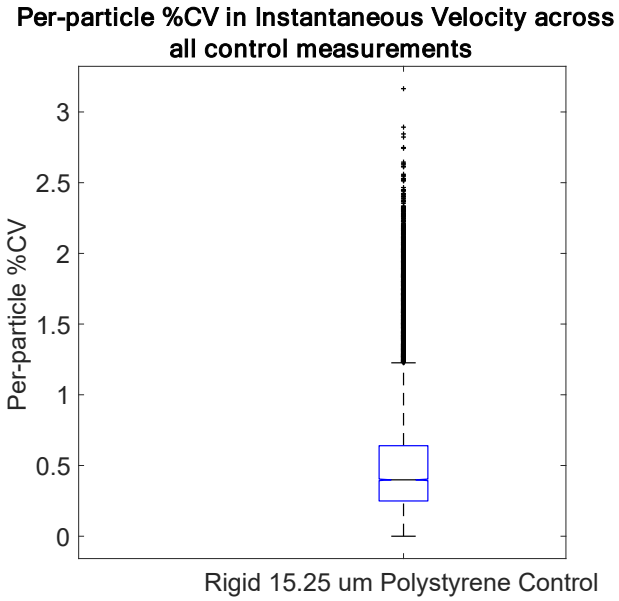

Figure S20: Per-particle CV in region 1 through 4 instantaneous velocity measurements for the rigid control population. Individual control particles CVs were grouped into one box from all runs. X-axis labels of elastic modulus (Pa, top row) and diameter (μm, bottom row) are nominal.

As with TOF, instantaneous velocity results showed greater variation and error among the control population at region 1 (Fig. S11) compared to regions 3 or 4 (Fig. S12). For any individual data collection, the greatest median instantaneous velocity difference for the control population—which is expected to be at 0 %—was -0.50 % for region 3 or 4. Out of all control particles, the IV_{rel} was always less than 1.5 % after outlier removal and for all particles at regions 3 and 4. The greatest standard deviation in the control population for any given run at regions 3 or 4 was 0.59 %. The standard deviation of IV_{rel} values of the control population was around 0.35 % for the second half of the device. For the first region, whose light profile was not as optimized for spectral signals analysis, the standard deviation of the control population was 1.3 %.

Across the experimental populations, the greatest variation in medians of instantaneous velocity among runs of the same particle lot was around a 5.0 % difference for the softest (0.1 kPa) particle lot at the first two regions (Fig. S13), a 3.5 % difference at region 3, and a 2.4 % difference at region 4 (Fig. S14). In general, run-to-run variations in instantaneous velocity decreased further down the chip and were mostly under 1.0 %. Variations also tended to be larger when the increase in instantaneous velocity was also larger compared to the control.

After grouping the same particle lot runs together, while region 1 and 2 populations had large standard deviations and wide ranges (Fig. S15), most standard deviations of population IV_{rel} were 5.0 % or less for regions 3 and 4 (Fig. S16). However, the softest particle population had up to 17 % standard deviation in IV_{rel} measurements. Despite the median being the largest for the softest particle group, this group, like others, also had negative values, or particles estimated to be slower velocities than the control. The instantaneous velocities were significant ($p < 0.001$) for all particle groups except the 1.2 and 1.1 kPa particles with mean diameters (17.5 ± 1.3) μm and (23.2 ± 3.0) μm, respectively, for region 4. Even though the medians were different for most populations, the spread of values were overlapping in most cases. At region 3, the values ranged from -15 % to 77 %. At region 4, this range was greater, from -18 % to 94 %, again indicating a possible increase in resolution later in the chip. Figure S17 shows a histogram view of the region 4 distributions, more clearly displaying how instantaneous velocity values do not distinguish populations well.

Precision on per-particle IV_{rel} measurements across all regions, which includes the two regions with poor measurement quality, was once again up to nearly 35 % CV for some individual particles (Fig. S18). The largest median per-particle IV_{rel} measurement CV for a lot was 13 %, although most lots had a median of under 10 %. That same lot had an upper adjacent per-particle CV of 30 %. Looking at just regions 3 and 4 in the device, the range between the two measurements of the same particle was a median of 10 % or less for any lot prior to outlier removal, although some particles had very large ranges due to the instantaneous nature of the metric (Fig. S19). In future iterations with the same waveguide for each region, the precision is likely to improve. For the control population, even looking across all four regions, the per-particle CV was under 3.0 % for almost all particles, and the upper adjacent was only 1.2 % (Fig. S20). Same-particle measurements of IV_{rel} for the control population at regions 3 and 4 differed by a range of under 1.7 % per particle, with an upper adjacent range of 0.6 %. In comparison, the

range was up to 6.0 % per-particle when including all regions, with an upper adjacent range of 2.7 %.

Unlike TOF, there did not appear to be a strong correlation between the population variation and either the mean or CV of the population elastic modulus or diameter.

Characterization of STA metrics: diameter

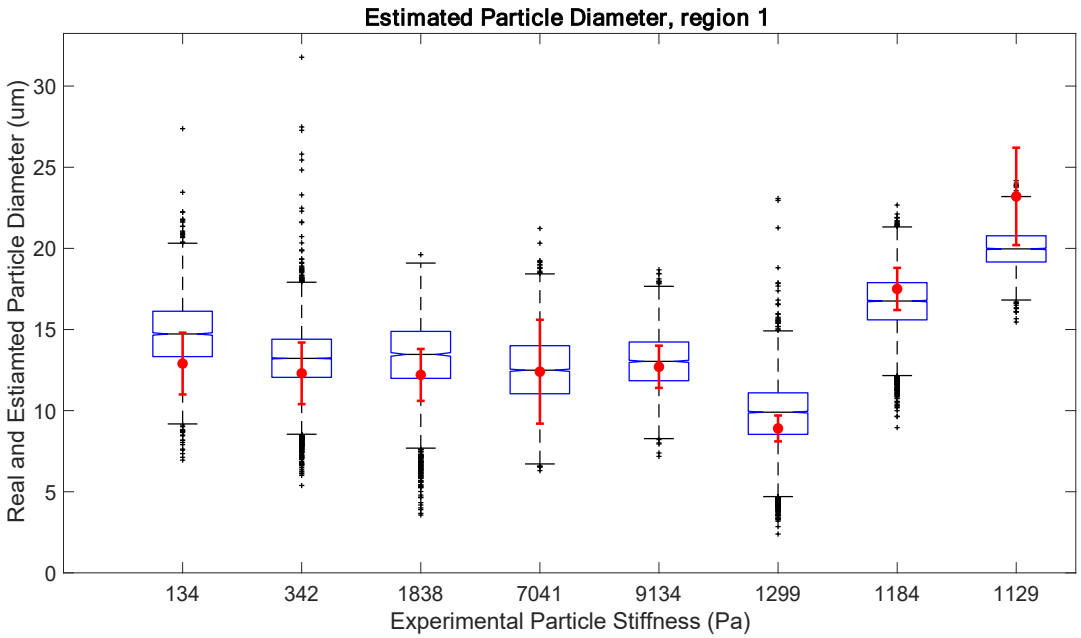

Figure S22: Particle diameters as estimated by STA (box and whisker) and as measured by microscopy (red). Error bars for red microscopy measurements represent one standard deviation. Particles are grouped by same lot. X-axis labels of elastic modulus (Pa) are nominal.

In the first two regions, particles much smaller or larger than the control did not have medians within the standard deviation of the actual size, again supporting the decision to exclude region 1 and 2 data due to particle instability (Fig. S22).

Comparison of metrics

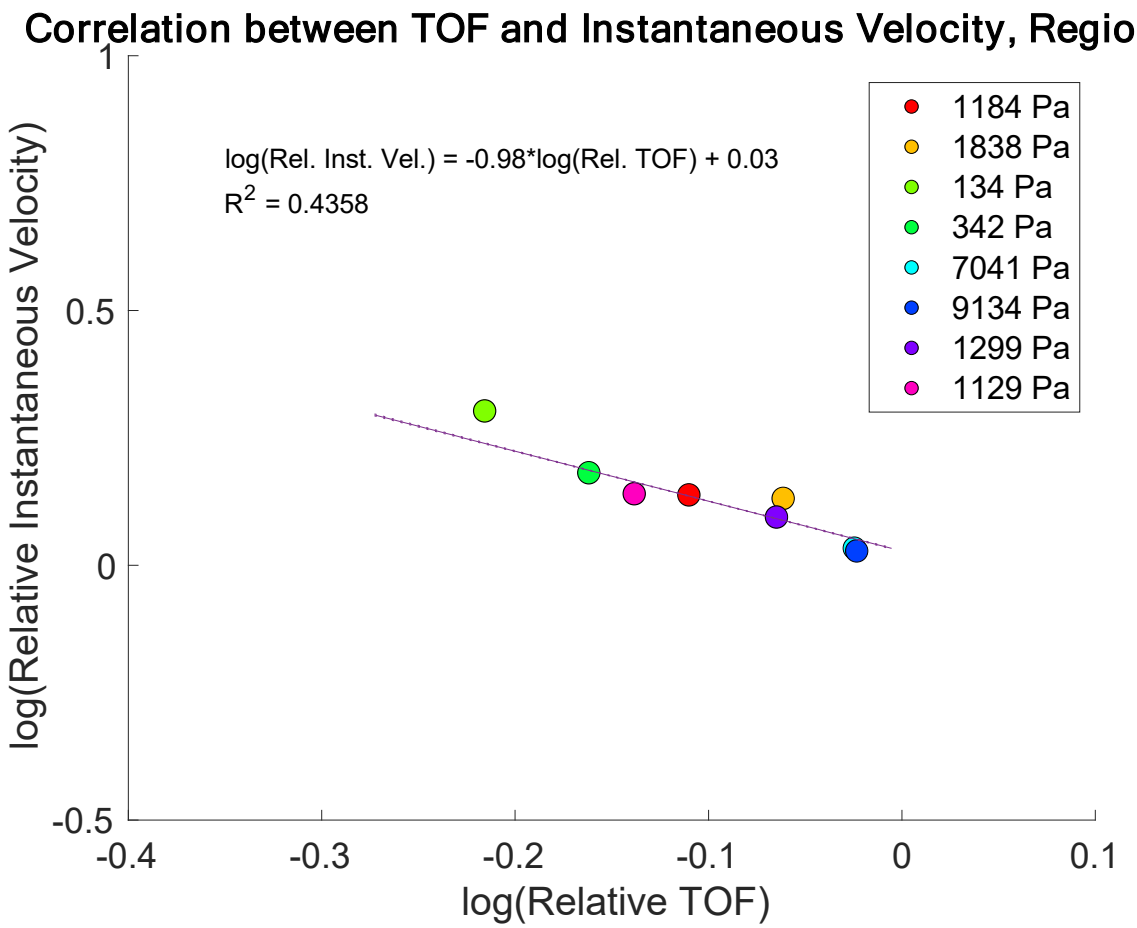

Figure S23: Correlation between the logged values of relative TOF and relative instantaneous velocity across all tested experimental particles. R^2 is 0.44. Values in legend are nominal.

Ideally, the instantaneous velocity and TOF measurements would be perfectly correlated. Instead, even at the most stable region 4, correlation between the two metrics across all experimental particles was only moderate, with an R^2 of 0.44 (Fig. S23). While variations in instantaneous velocity are much larger than in TOF, the relationship specifically of size/modulus to instantaneous velocity is neither as strong nor as sensitive as size/modulus to TOF, as TOF is far more robust to random error and instantaneous fluctuations.

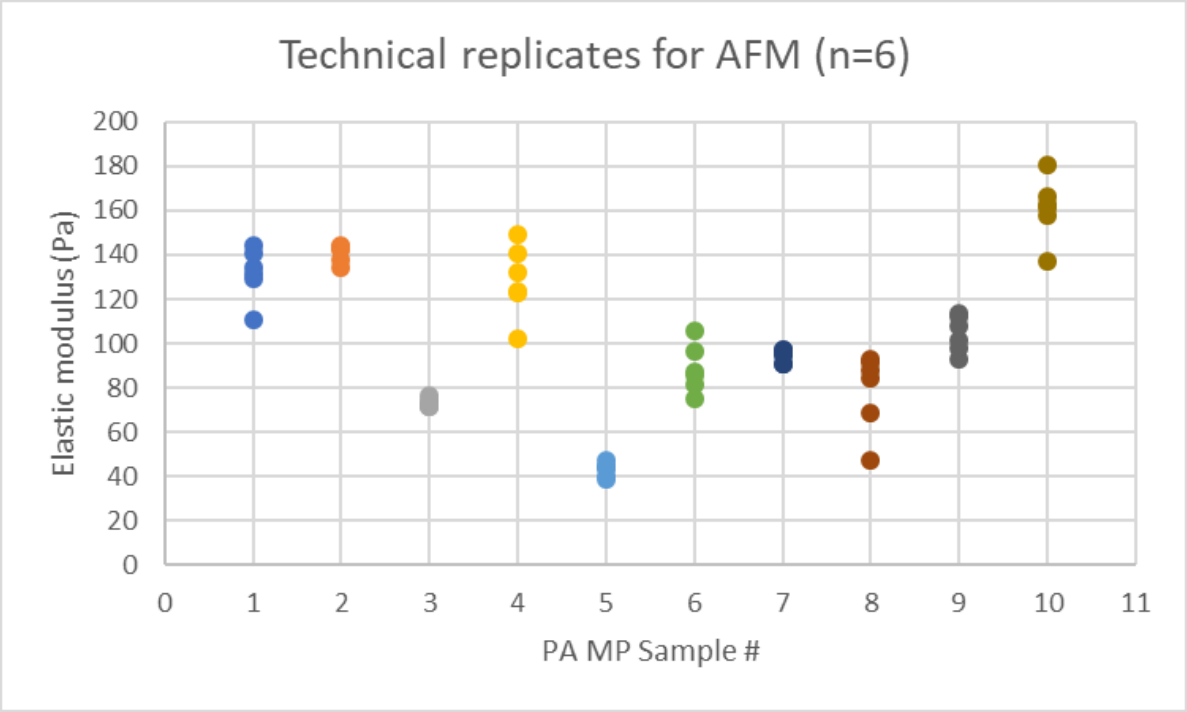

Figure S24: Technical replicates of (104 ± 36) Pa polyacrylamide particles on AFM. Each of the ten particles was tested six times. Per-particle CVs range from (2.8 - 22.6) %, with a mean 9 % CV.